

Supplemental Material for

An explosive volcanic origin identified for dark sand in Aeolis Dorsa, Mars

Devon M. Burr

Astronomy and Planetary Science Department
Northern Arizona University
Flagstaff AZ 86011, US

Christina E. Viviano

Space Exploration Sector,
Johns Hopkins University Applied Physics Laboratory,
Laurel, MD 20723, US

Timothy I. Michaels

SETI Institute
Mountain View, CA 94043, US

Matthew Chojnacki

Planetary Science Institute
Lakewood, CO 80401, US

Robert E. Jacobsen

Earth and Planetary Sciences Department,
University of Tennessee-Knoxville
Knoxville, Tennessee 37996, US

Contents of this file:

- Methods Text, including Table S1, Methods Figure 1, and References
- Supplemental Figures S1-S3 with Captions and References
- Captions for Supplemental information uploaded separately:
 - Animation S1
 - Datasets 1 and 2 in Excel format
 - ArcGIS geodatabase with layer files
 - CRISM browse products
 - ArcGIS geodatabase with locations of grain size derivation

Methods

Locations of sand deposits and inferred wind directions from mapping:

We used mapping to both determine locations of sand deposits and infer the wind directions that most recently mobilized those deposits. Exposed Aeolis Dorsa sand deposits appear visually dark and thermally bright (Burr et al., 2011). Thus, we mapped dark sand using imaging data from both the MRO Context Camera (CTX) (5-6 m/pixel; Malin et al., 2007; Dickson et al., 2018) and the Mars Odyssey's Thermal Emission Imaging System (THEMIS) daytime and nighttime infrared mosaics (100 m/pixel; Christensen et al., 2004). In some visually bright plains, dust-covered sand deposits are inferred from moats, interpreted as scour marks or echo dunes around flow obstacles (Bishop 2011). Because thick dust cover prohibits the use of spectroscopy for comparing sand mineralogy to possible source regions, these areas were not mapped in this work.

To identify sand deposits, we derived threshold data number (DN) values indicative of dark sand for each mosaic. In the two THEMIS mosaics, DN values greater than 130 were considered evidence for sand, based on visual inspection of and correlation with transition regions between visually dark and visually bright (dust-covered) sand. In the blended CTX global mosaic (Dickson et al., 2018), DN values less than 110 were considered evidence for dark sand. This value was derived empirically from visual inspection of transitions between sand inferred to be predominately dust-covered (as evidenced by scour marks or dust devil tracks) and sand inferred to be predominately dust-free (commonly associated with meter-scale ripples).

After identification, dark sands were delineated as ArcGIS polygons on the CTX mosaic because of its high spatial resolution at the mapping scale of 1:25,000. To create contiguous units of dark sand, some areas mapped as dark sands include some bright outcrops of bedrock or dusty rippled deposits, which comprise a minority of the polygon. The "dark sands" polygon file was then ingested into the Line Density ArcGIS tool (<https://desktop.arcgis.com/en/arcmap/latest/tools/spatial-analyst-toolbox/line-density.htm>) producing a magnitude-per-unit area (km²) file that highlighted the seven densest sub-regions in the study area for further analysis.

All areas mapped as having dark sands were then examined for wind-orientation indicators. For this examination, we used the CTX mosaic and available images from MRO's High Resolution Imaging Science Experiment (HiRISE) camera (McEwen et al., 2007). Whereas the CTX mosaic provides nearly continuous coverage of the study area, HiRISE image pixels have greater spatial resolution (0.3 m/pixel) and dynamic range, which were particularly helpful for discerning the shapes and orientations of aeolian features.

We identified and analyzed two unidirectional and two bidirectional wind indicators. Unidirectional indicators include scour marks and simple dunes including barchan dunes and collectively referred to here as duneforms. Scour marks (or current crescents) are roughly semicircular flat moats on the upward sides of obstacles (Bishop, 2011). The orientation of the scour-forming wind was measured as the direction perpendicular to a line connecting both ends of the scour mark. Simple dunes such as barchans and barchanoids are crescent-shaped aeolian

features with asymmetric slopes, the steeper slope being the downwind surface and on the concave side of the dune (Lancaster, 2009). Similar crescentic dunes termed echo dunes (Greeley and Iverson, 1985) were also commonly found anchored against yardang or butte bases. The dune-forming wind orientation was measured perpendicular to a line connecting both ends of the dune (Fenton et al., 2003). Duneforms mapped here were distinguished from light-toned transverse aeolian ridges (TARs) by albedo, size and shape. TARs are relatively static landforms (10-100 m spacing), which are possibly armored megaripples (e.g., Foroutan & Zimbelman, 2016; and refs. therein). Because TARs were interpreted as ancient landforms due to dust accumulation and occasional superposed impact craters, they were deemed not representative of modern winds and so not included in the analysis.

Bidirectional aeolian features, for which the formational wind could only be constrained to two opposing directions, included dark-toned ripples and dust devil tracks. On Mars most duneforms and sand sheets are mantled in dark-toned ripples with spacings of 1-5 m and typically arranged in a transverse pattern (see below) (Bridges et al., 2007). Meter-spaced ripples with a consistent orientation were mapped with lines perpendicular to their crests. In cases where ripples near the summit of a dune are parallel to a nearby slipface, greater confidence can be taken that formation winds were toward the slipface. Nevertheless, the more conservative 180° ambiguity was applied to ripples. TARs and smaller ripples which were partially coated in light-toned dust were not mapped.

Dust devil tracks are relatively dust-free swaths of sediment, cleaned of dust by wind shear and grain impacts during passing vortices (Cantor et al., 2006; Verba et al., 2010). Track-forming wind orientations were measured parallel to the orientations of tracks. Concentrations of relatively straight tracks were favored over those that were curved or meandering.

ArcMap tools were used to calculate and display statistics for wind-orientation indicators. We joined the polygons outlining areas of dark sands to shapefiles representing each of the four indicator types and, in doing so, derived the number of indicators per unit area (km²) and calculated the average and standard deviation of the orientations. This information was then converted to points for representation as arrows with orientations corresponding to the average orientation (by type) and the labeling representing the standard deviation of orientations. The sizes of the arrows are scaled to the number of indicators per square kilometer of dark sand, providing a weighting function. For example, a given sand deposit may have a dozen or more ripple orientation measurements that collectively represent one arrow's direction whereas its size reflects the sand deposit's area.

Derivation of sand grain sizes:

As the thermal inertia values of unconsolidated surfaces are largely controlled by grain size, they can be used to estimate effective grain sizes, particularly for well-sorted sediments of dunes and sand patches. Martian thermal inertia values are commonly derived from nighttime temperatures (Christensen et al., 2001; Jakosky et al., 2006), including ~100 m/pixel from Mars Odyssey's Thermal Emission Imaging System (THEMIS) temperature images (Christensen et al., 2004; Fergason et al., 2006). For this work, we followed the approach of Chojnacki et al. (2014) in deriving thermal inertia ($\text{J m}^{-2} \text{K}^{-1} \text{s}^{-1/2}$) values using THEMIS predawn band 9 (12.57 μm)

brightness temperature images in coordination with a seven-dimensional lookup table of temperatures based on season, time of day, latitude, surface pressure, dust opacity, albedo, and thermal inertia (Putzig and Mellon, 2007 and references therein). The table was interrogated with the brightness temperatures in correlation with the other datasets to find the best-fit (interpolated) thermal inertias.

From these thermal inertia values, we calculated best-fit grain sizes using a lookup table from Piqueux and Christensen (2009), under the assumption of a homogenous mono-modal dry and ice-free distribution of sediment. Inputs to the table were atmospheric pressures and our THEMIS thermal inertia and surface temperature measurements, with constant porosity and thermal conductivity (for basaltic sand) of 36% and $0.058 \text{ W m}^{-1} \text{ K}^{-1}$, respectively (Presley and Christensen, 1997; Piqueux and Christensen, 2009). Using this approach, we estimated effective grain sizes using hundreds of THEMIS thermal inertia pixels for contiguous, frequently rippled, sandy areas that appeared homogenous and devoid of rock outcrops in HiRISE or CTX images. The results are shown in the table below.

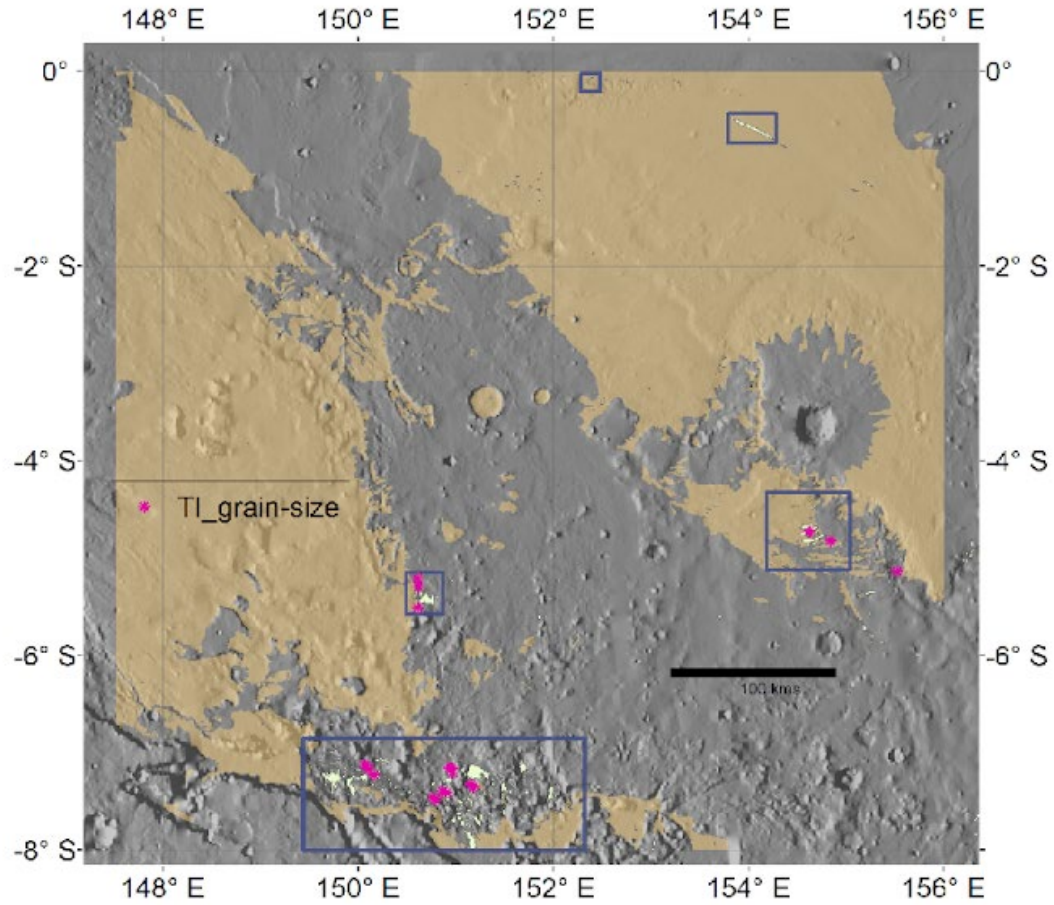
Table S1. Thermal inertia and grain size analysis. For SubArea locations, see either Figure 1C or Figure below.					
THEMIS QUB	center_lon	center_lat	SubArea	TI (tiu) mean \pm std^a	Psize^b
I05469005	150.623	-5.295	E Aeolis Planum	215 \pm 32	0.35 mm
I18299010	150.164	-7.225	Aeolis Chaos	181 \pm 16	0.18 mm
I18299010	150.109	-7.169	Aeolis Chaos	160 \pm 19	0.10 mm
I18299010	150.075	-7.124	Aeolis Chaos	100 \pm 12	0.02 mm
I08053012	150.940	-7.151	Aeolis Chaos	240 \pm 25	0.43 mm
I08053012	151.183	-7.357	Aeolis Chaos	270 \pm 22	0.77 mm
I08053012	150.965	-7.161	Aeolis Chaos	262 \pm 27	0.65 mm
I08053012	150.973	-7.206	Aeolis Chaos	280 \pm 33	0.94 mm

I08053012	150.870	-7.395	Aeolis Chaos	198 ± 21	0.19 mm
I08053012	150.906	-7.411	Aeolis Chaos	233 ± 28	0.37 mm
I08053012	150.797	-7.483	Aeolis Chaos	207 ± 24	0.22 mm
I08053012	150.611	-5.509	E Aeolis Planum	167 ± 18	0.10 mm
I08053012	150.614	-5.210	E Aeolis Planum	180 ± 19	0.13 mm
I17363010	150.769	-7.462	Aeolis Chaos	236 ± 20	0.49 mm
I06842006	154.629	-4.729	Southern Zephyria Planum	215 ± 29	0.31 mm
I07204007	154.848	-4.823	Southern Zephyria Planum	180 ± 15	0.14 mm
I0829001	155.531	-5.137	Southern Zephyria Planum	222 ± 31	0.32 mm
I08078012	151.162	-7.323	Aeolis Chaos	315 ± 39	1.80 mm

^aTHEMIS thermal inertia in units of $\text{Jm}^{-2}\text{K}^{-1}\text{s}^{-1/2}$ (see text for description).

^bEffective grain sizes were derived from THEMIS thermal inertia values, following the method of *Piqueux and Christensen* [2009] (see text for description). Absolute error is estimated to be ~10%.

Methods Figure 1. Locations for grain size analysis derived from thermal inertia data in Table S1 above. As on Figure 1C, plana units are in tan, sand deposits are in light green, and the locations of sand-rich areas, as shown on Figure 1C and Figure S3(C-G) images, are indicated by blue boxes.



Composition of sand from CRISM analysis:

Data from the Compact Reconnaissance Imaging Spectrometer for Mars (CRISM) (Murchie et al., 2007) on board the MRO (Zurek and Smrekar, 2007) were used for the compositional analysis in this work. The Map-projected Targeted Reduced Data Record (MTRDR) products, derived by processing CRISM hyperspectral targeted (18m/pix) observations through a series of spectral corrections, data projection, and summary product rendering, were exclusively used for detailed spectral analysis. The corrected 'I/F' data (a ratio of the radiance observed by the CRISM instrument to the solar irradiance incident at the top of the Martian atmosphere) were derived via a standard photometric correction, followed by an updated "volcano scan" atmospheric correction (Bibring et al., 1989; Langevin et al., 2005; McGuire et al., 2009) that accommodates for subtle shifts in the wavelength calibration (Morgan et al., 2011). Empirical corrections for "spectral smile" (cross-track shifts in the wavelength calibration) and characteristics related to a varying observation geometry and atmospheric path length are also applied (Seelos et al., 2011). Data from the visible/near-infrared detector (0.4-1.0 μm) are joined to data from the infrared detector (1.0-4.0 μm) creating a fully 'joined' spectral cube (Seelos et al. 2012). Data from both detectors were required for compositional analysis across the 1- μm region performed here. Standard spectral parameters were calculated and applied to the hyperspectral image cubes (Viviano-Beck et al., 2014) to highlight spectral and compositional variability within each scene.

We selected CRISM data for this work by surveying available products throughout the four potential source regions -- the southern highlands, Cerberus plain, Elysium Mons, and Aeolis Dorsa -- for localized potential sand sources. These potential sand sources are listed in the Attribute Table for the CRISM_mapping File Geodatabase Feature Class provided in the Supplemental Online Materials. In the Attribute Table under Localized Potential Sand Sources, the first two letters designate the region (AD = Aeolis Dorsa, SH = southern highlands, Cp = Cerberus plains, EM = Elysium Mons), the subsequent word(s) indicate the generic potential sand source (e.g., impact crater, slope, fissure, deposit), and following any text in parentheses provides additional information (e.g., tone, size of crater). Ninety-seven unique CRISM MTRDR observations were analyzed across all four potential sand source regions. This total includes all available images with data from both detectors in the AD study area (0 - 8S, 147.5 - 156E) and a representative number of images from each of the other three possible sand source regions.

Combinations of these spectral parameters were used to identify locations where non-dusty surfaces were present in the study region. Of the 97 MTRDR images analyzed, 56 revealed non-dusty spectral signatures as indicated by a combination of spectral parameters sensitive to variations in the 1- μm region (e.g., OLINDEX3, BD1300, BDI1000VIS, BDI1000IR) and confirmed by extracting spectra from these locations. From these 56 images, we extracted spectra from 197 locations to assess for contributions from iron-bearing minerals using the broad 1- μm band associated with iron-content in mafic minerals including pyroxene (PYX), olivine (OL), and Fe-bearing glass (GLS). The position of the 2- μm band in pyroxene was also used to differentiate between low-calcium (LCP) and high-calcium pyroxene (HCP). First described in Horgan et al. (2014) and then utilized for Amazonian surfaces in Viviano et al. (2019), the 1- μm asymmetry, 1- μm band center, and 2- μm band center for these locations were determined using the methods of Viviano et al. (2019) to classify Fe-bearing composition as one of seven

compositional mixtures or endmembers. Individual spectra exhibiting non-dust spectral features were ratioed to nearby dusty material imaged in the same detector column to mitigate column-dependent systematic noise and highlight non-dust spectral features (Murchie et al., 2009). The location of extracted spectra from pixels in the unprojected image that were averaged and ratioed are provided in the supplementary materials. Band centers were calculated by determining the inflection point between the 1- and 2- μm bands, using the RPEAK1 CRISM parameter value to set the position of the shorter shoulder for the 1- μm band, and 2.5 μm set as the position of the longer shoulder for the 2- μm band. These shoulders were used to model a continuum and fit a Gaussian curve to the resulting continuum-removed spectrum to determine band centers. The 1- μm asymmetry was defined as the area to the right of the band center minus the area to the left of the band center, expressed as a percentage. See Viviano et al. 2019 for a detailed explanation of the band modeling.

We bin the seven compositional groups in the 1- μm asymmetry vs. 1- μm center space into the following: pyroxene (LCP, HCP, and LCP/HCP mixtures), mafic mixtures (pyroxenes mixed with olivine/glass, glass, or olivine/glass mixtures), and olivine (Fe or Mg-bearing). Alteration minerals were also noted when present using a combination of spectral parameters (e.g., BD1900_2, D2300, BD2290, SINDEX2) and extracted spectra to identify based on band shape and position (see Viviano-Beck et al. 2014 and references therein).

The values plotted in Figure 2 (“Spectra for potential source regions”) were derived via the methods outlined in Viviano et al. 2019. Ferrous mineral mixtures are classified using this plot into groups each consistent with one or more mixtures of phases shown by the colored domains: pyroxene-dominated (green and blue zones), mixtures of pyroxene, olivine, and/or glass (orange, yellow, and pink zones), and olivine-dominated (red zone).

Potential sand flux from modeling:

To estimate potential sediment transport magnitudes and directions over the four potential sand source regions and throughout the study area, simulations were performed with the Mars Regional Atmospheric Modeling System (MRAMS; Rafkin et al. 2001, Rafkin and Michaels 2019). Output from the Mars global climate model (Haberle et al. 2019) with ~ 300 km horizontal grid spacing was used to provide the initial state and time-dependent lateral boundary conditions. A series of six nested MRAMS grids (each with a successively smaller total area and horizontal grid spacing) was then used to investigate regional sediment transport pathways. The grid encompassing the Elysium Mons complex, the Cerberus plains, the detailed study area, and the adjacent southern highlands used a grid spacing of < 16.5 km. The detailed study area was covered by a mesh with a grid spacing of < 2.78 km, in order to investigate more-local potential sediment transport and to better compare to the observed orientations of mapped aeolian deposits. MRAMS runs (each 2 sols in duration) were performed for twelve seasonal L_s windows (every 30°) to resolve seasonal variability, centered on L_s 10° , 40° , ... 340° . We use present-day obliquities, as the low albedo of the dark dunes suggests limited dust cover and dust storms occur frequently in this location at the current obliquities. And although with current data coverage we didn’t detect sand motion on Aeolis or Zephyria Plana, the subtle ripple motion in the Aeolis Chaos (Animation DR1) documents current sand motion within the study area.

The potential sediment mass flux is the maximum possible flux (assuming always-available sand grains) and represents the mass per unit time that moves across a meter-long distance perpendicular to the wind -- its calculation follows the method described in Stillman et al. 2021, which is largely reiterated below. Estimated annual potential sediment transport values were calculated at each MRAMS grid point using model output fields and the saltation mass flux expression preferred by Kok et al. (2012). To determine if winds were strong enough to induce sediment transport at a given instant and grid point, the modeled shear velocity u^* (conceptually, the speed at which the air pushes against the taller surface roughness elements) was compared to the associated fluid threshold u_{*f}^* and/or impact threshold u_{*it}^* . The fluid threshold is the shear velocity at which saltation is initiated and depends on the properties of the fluid, particles (sand grains), gravity, and interparticle cohesion forces (Kok et al. 2012). Here the u_{*f}^* values were calculated using the semi-empirical expressions of Greeley and Iversen (1985), using an interparticle cohesion parameter of $6 \times 10^{-7} \text{ N m}^{-0.5}$ (as in Lorenz et al. 1995, Newman et al. 2002) and a grain mass density of 2400 kg m^{-3} . The minimum u_{*f}^* for each given condition was used, corresponding to a grain diameter of $\sim 100 \text{ }\mu\text{m}$. The impact threshold is the shear velocity at which saltation can be sustained and takes into account the extra momentum that already-saltating grains impart upon impact with grains still on the ground. On Earth $u_{*it}^* \sim 0.8 u_{*f}^*$, but on Mars $u_{*it}^* \sim 0.1 u_{*f}^*$ due to the lower gravity and different atmospheric composition and density (Kok 2010). This low impact threshold indicates that on Mars once saltation has started somewhere upwind, more moderate winds can sustain saltation until gusts no longer exceed u_{*it}^* .

MRAMS computes the spatial-mean wind (within each 3-D grid cell) at any given time, but there are also smaller-scale winds that are unresolved (e.g., Bridges et al. 2012). These unresolved winds can be represented as a probability distribution function (PDF; Fenton and Michaels 2010). The PDF of small-scale winds generally becomes more widely distributed with greater turbulence. Therefore, if turbulence is sufficiently vigorous, a wind gust exceeding the fluid threshold may occur even when the MRAMS spatial-mean $u^* < u_{*f}^*$. Thus, saltation should be expected to begin within a mesoscale model simulation either when $u^* \geq u_{*f}^*$ or when $u^* \geq u_{*it}^*$ and the atmosphere is sufficiently turbulent. In order to parameterize the width of the PDF which represents the probability of unresolved small-scale wind gusts with $u^* \geq u_{*f}^*$ at any given time, we used the bulk surface layer Richardson number Ri_{Bsl} (e.g., Arya 1988). Ri_{Bsl} is effectively a ratio between the production (or inhibition) of turbulence via buoyancy (i.e., less-dense air parcels rising) and via mechanical means (i.e., due to the tendency of faster-moving air parcels to mix with adjacent slower-moving air parcels; proportional to vertical wind shear). When $Ri_{Bsl} < 0$, air parcels warmed by the ground will rise and produce more vigorous turbulence, even if there is little or no wind. When $Ri_{Bsl} > 0$, the buoyancy forces begin to inhibit turbulence that any wind shear may be generating. Increasing the wind magnitude (and thus wind shear) results in a steep reduction of the absolute magnitude of Ri_{Bsl} , so very small values of Ri_{Bsl} also indicate relatively robust turbulence. Therefore, when $Ri_{Bsl} < 0.03$, we assume that the unresolved wind PDF is broad enough to allow saltation when the modeled $u^* \geq u_{*it}^*$.

At each MRAMS grid point, the resulting potential sediment mass fluxes from the final simulated sol were binned into 16 equally-spaced direction bins. Within each L_s window and direction bin, the instantaneous estimates of potential sediment mass flux were integrated with respect to time to obtain the daily potential sediment transport (kg m^{-1} per sol). Those values were then multiplied by the number of actual sols encompassed by each L_s window to obtain the

potential sediment transport in each window. These values were then summed, yielding the annual potential sediment transport (kg m^{-1} per Mars-year) in each direction bin at each MRAMS grid point.

Survey for potential sand sources in HiRISE images:

To identify any local-scale potential sand sources in the study region, we surveyed all HiRISE images (McEwen et al. 2007) available through December 2020. The images were viewed in HiView for characteristics consistent with a local sand source. These characteristics were:

1. Lower albedo area compared to higher elevation surroundings. This gateway criterion was assessed quantitatively ($\text{DN} < 100$ or > 50 DN different from surroundings) in HiVIEW. To circumvent the effect of shadowing, we endeavored to collect data from slopes orthogonal to illumination.
2. On an apparent slope
3. Fine-grained sedimentary appearance: low-albedo area has fan, bajada, and/or slope streak shape
4. Exhibiting vertical striations with a few-meter wavelength suggestive of megaripples
5. Connected to a possible source feature, either a capping layer or low-albedo stratum within slope or an alcove or fissure in a yardang wall.

Locations exhibiting four or five of these five characteristics were considered potential sand sources (PSSs).

We initially surveyed all HiRISE images in the study area for PSSs. These PSS identifications throughout the study area were then reviewed and filtered for only PSSs over mapped Plana units (Burr et al., 2021) coincident with MFF. Lastly, we grouped the highest confidence PSS identifications. The Supplementary Information (Burr_etal_AeolisDorsa_PSS-survey_HiRISE) provides final results of this downselection process including screen captures of the highest confidence PSS identifications on Plana units and comments. Some HiRISE images had numerous PSSs and the images of PSSs for each HiRISE image recorded in this spreadsheet may not be exhaustive.

Data availability: Topographic data used in this work, including for the potential sand transport modeling, are available either at [Mars MGS MOLA - MEX HRSC Blended DEM Global 200m v2](#) or [PDS Geosciences Node Data and Services: MGS MOLA MEGDRs](#)

The THEMIS day and night mosaics are available at [Mars THEMIS Controlled Mosaics and Final Smithed Kernels](#) The Context Camera data are available at [Mars CTX \(beta01\) Image Mosaic - Overview](#). The HiRISE data are available at [HiRISE | High Resolution Imaging Science Experiment](#) or [Mars HiRISE Image Mosaic - Overview](#). The CRISM data are available at [PDS Geosciences Node Data and Services: MRO CRISM](#) and the reduced data (CRISM browse products) are available in the Supplemental Information materials. The data analysis results (including the extracted spectra) that support the findings of this study are available from the corresponding author upon reasonable request.

References for Methods:

Bibring, J.-P., et al. (1989). Results from the ISM experiment, *Nature*, 341(6243), 591–593, doi:10.1038/341591a0.

Bishop, M. A. (2011). Aeolian scours as putative signatures of wind erosion and sediment transport direction on Mars. *Geomorphology*, 125(4), 569–574.
<https://doi.org/10.1016/j.geomorph.2010.10.029>

Bridges, N. T., Geissler, P. E., McEwen, A. S., Thomson, B. J., Chuang, F. C., Herkenhoff, K. E., et al. (2007). Windy Mars: A dynamic planet as seen by the HiRISE camera. *Geophysical Research Letters*, 34(23). <https://doi.org/10.1029/2007GL031445>

Burr, D.M., J. R. Zimbelman, F. B. Qualls, M. Chojnacki, S. Murchie, T. I. Michaels (2011). The western Medusae Fossae Formation: a source of dark aeolian sand on Mars. *Lunar Planet. Sci. XLI* (abstract 1582).

Cantor, B. A., Kanak, K. M., & Edgett, K. S. (2006). Mars Orbiter Camera observations of Martian dust devils and their tracks (September 1997 to January 2006) and evaluation of theoretical vortex models. *J. Geophys. Res.*, 111(E12), E12002.
<https://doi.org/10.1029/2006JE002700>

Chojnacki, M., Burr, D. M., & Moersch, J. E. (2014). Valles Marineris dune fields as compared with other martian populations: Diversity of dune compositions, morphologies, and thermophysical properties. *Third Planetary Dunes Systems*, 230(0), 96–142.
<https://doi.org/10.1016/j.icarus.2013.08.018>

Christensen, P.R. et al., (2001). Mars Global Surveyor Thermal Emission Spectrometer experiment: Investigation description and surface science results: *Journal of Geophysical Research*, v. 106, p. 23823–23871, doi:10.1029/2000JE001370.

Christensen, P. R., Jakosky, B. M., Kieffer, H. H., Malin, M. C., McSween, Jr., H. Y., Nealson, K., et al. (2004). The Thermal Emission Imaging System (THEMIS) for the Mars 2001 Odyssey Mission. *Space Science Reviews*, 110(1/2), 85–130.
<https://doi.org/10.1023/B:SPAC.0000021008.16305.94>

Dickson, J. L., Kerber, L. A., Fassett, C. I., & Ehlmann, B. L. (2018). A Global, Blended CTX Mosaic of Mars with Vectorized Seam Mapping: A New Mosaicking Pipeline Using Principles of Non-Destructive Image Editing. In *49th Lunar and Planetary Science Conference* (p. Abstract #2480). Houston: Lunar and Planetary Institute. Retrieved from <http://www.lpi.usra.edu/meetings/lpsc2018/pdf/2480.pdf>

Fenton, L. K., Bandfield, J. L., & Ward, A. W. (2003). Aeolian processes in Proctor Crater on Mars: Sedimentary history as analyzed from multiple data sets. *Journal of Geophysical Research*, 108(E12). <https://doi.org/10.1029/2002JE002015>

Ferguson, R.L., Christensen, P.R., and Kieffer, H.H., (2006). High-resolution thermal inertia derived from the Thermal Emission Imaging System (THEMIS): Thermal model and applications: *Journal of Geophysical Research*, v. 111, doi:10.1029/2006JE002735.

Foroutan, M., & Zimbelman, J. R. (2016). Mega-ripples in Iran: A new analog for transverse aeolian ridges on Mars. *Icarus*, 274, 99–105. <https://doi.org/10.1016/j.icarus.2016.03.025>

Greeley, R., & Iversen, J. D. (1985). In R. Greeley (Ed.), *Wind as a geological process on Earth, Mars, Venus and Titan* (p. 332). New York: Cambridge University Press.

Hayward, R. K., Fenton, L. K., & Titus, T. N. (2014). Mars Global Digital Dune Database (MGD3): Global dune distribution and wind pattern observations. *Icarus*, 230(0), 38–46. <https://doi.org/10.1016/j.icarus.2013.04.011>

Horgan, B.H.N., Cloutis, E.A., Mann, P., Bell, J.F., (2014). Near-infrared spectra of ferrous mineral mixtures and methods for their identification in planetary surface spectra. *Icarus* 234, 132–154.

Jakosky, B.M., Hynek, B.M., Pelkey, S.M., Mellon, M.T., Martinez-Alonso, S., Putzig, N.E., Murphy, N., and Christensen, P.R., (2006). Thermophysical properties of the MER and Beagle II landing site regions on Mars: *J. Geophys. Res.*, v. 111, p. E08008.

Lancaster, N. (2009). Dune Morphology and Dynamics. In Anthony J. Parsons & Athol D. Abrahams (Eds.), *Geomorphology of Desert Environments* (pp. 557–595). Chapter 18: Springer Netherlands. Retrieved from http://dx.doi.org/10.1007/978-1-4020-5719-9_18

Langevin, Y., F. Poulet, J.-P. Bibring, and B. Gondet (2005). Sulfates in the north polar region of Mars detected by OMEGA/Mars Express, *Science*, 307(5715), 1584–1586, doi:10.1126/science.1109091.

Malin, M. C., Bell, J. F., Cantor, B. A., Caplinger, M. A., Calvin, W. M., Clancy, R. T., et al. (2007). Context Camera Investigation on board the Mars Reconnaissance Orbiter. *Journal of Geophysical Research*, 112(E5). <https://doi.org/10.1029/2006JE002808>

McEwen, A. S., Eliason, E. M., Bergstrom, J. W., Bridges, N. T., Hansen, C. J., Delamere, W. A., et al. (2007). Mars Reconnaissance Orbiter's High Resolution Imaging Science Experiment (HiRISE). *Journal of Geophysical Research*, 112(E5). <https://doi.org/10.1029/2005JE002605>

McGuire, P. C., et al. (2009). An improvement to the volcano-scan algorithm for atmospheric correction of CRISM and OMEGA spectral data, *Planet. Space Sci.*, 57(7), 809–815, doi:10.1016/j.pss.2009.03.007.

Morgan, F., J. F. Mustard, S. M. Wiseman, F. P. Seelos, S. L. Murchie, P. C. McGuire, and C. Team (2011). Improved algorithm for CRISM volcanoscan atmospheric correction, *Lunar Planet. Inst. Sci. Conf. Abstr.*, 42, 2453. [Available at <http://adsabs.harvard.edu/abs/2011LPI...42.2453M>.]

Murchie, S., R. Arvidson, P. Bedini, K. Beisser, J.-P. Bibring, J. Bishop, J. Boldt, P. Cavender, T. Choo, R. T. Clancy, E. H. Darlington, D. Des Marais, R. Espiritu, D. Fort, R. Green, E. Guinness, J. Hayes, C. Hash, K. Heffernan, J. Hemmler, G. Heyler, D. Humm, J. Hutcheson, N. Izenberg, R. Lee, J. Lees, D. Lohr, E. Malaret, T. Martin, J. A. McGovern, P. McGuire, R. Morris, J. Mustard, S. Pelkey, E. Rhodes, M. Robinson, T. Roush, E. Schaefer, G. Seagrave, F. Seelos, P. Silvergate, S. Slavney, M. Smith, W.-J. Shyong, K. Strohbehn, H. Taylor, P. Thompson, B. Tossman, M. Wirzburger, and M. Wolff. 2007. 'Compact Reconnaissance Imaging Spectrometer for Mars (CRISM) on Mars Reconnaissance Orbiter (MRO)', *Journal of Geophysical Research (Planets)*, 112, E05S03
<https://doi.org/10.1029/2006JE002682>.

Murchie, S.L., Seelos, F.P., Hash, C.D., Humm, D.C., Malaret, E., McGovern, J.A., Seelos, K.D., Buczkowski, D.L., Morgan, M.F., Barnouin, O.S., Nair, H., Taylor, H.W., Patterson, G.W., Harvel, C.A., Mustard, J.F., Arvidson, R.E., McGuire, P., Smith, M.D., Wolff, M.J., Titus, T.N., CRISM Science Team, (2009). The CRISM investigation and data set from the Mars Reconnaissance Orbiter's Primary Science Phase. *J. Geophys. Res.* 114, E00D07.

Piqueux, S., and Christensen, P.R., (2009). A model of thermal conductivity for planetary soils: 1. Theory for unconsolidated soils: *Journal of Geophysical Research*, v. 114, doi:10.1029/2008JE003308.

Presley, M.A., and Christensen, P.R., (1997). Thermal conductivity measurements of particulate materials 2. Results: *Journal of Geophysical Research*, v. 102, p. 6551–6566, doi:10.1029/96JE03303.

Putzig, N., and Mellon, M., (2007). Apparent thermal inertia and the surface heterogeneity of Mars: *Icarus*, v. 191, p. 68–94, doi:10.1016/j.icarus.2007.05.013.

Seelos, F. P., S. L. Murchie, D. C. Humm, O. S. Barnouin, F. Morgan, H. W. Taylor, C. Hash, and C. Team (2011). CRISM data processing and analysis products update — Calibration, correction, and visualization, *Lunar Planet. Inst. Sci. Conf. Abstr.*, 42, 1438.

Seelos, F. P., M. F. Morgan, H. W. Taylor, S. L. Murchie, D. C. Humm, K. D. Seelos, O. S. Barnouin, C. E. Viviano, and C. R. I. S. M. Team (2012). CRISMMAP Projected Targeted Reduced Data Records (MTRDRs) – High level analysis and visualization data products, in *Planetary Data: A Workshop for Users and Software Developers*, U.S. Geological Survey, Reston, Va.

Seelos, K. D., Seelos, F. P., Viviano-Beck, C. E., Murchie, S. L., Arvidson, R. E., Ehlmann, B. L., & Fraeman, A. A. (2014). Mineralogy of the MSL Curiosity landing site in Gale crater as observed by MRO/CRISM. *Geophysical Research Letters*, 41(14), 4880–4887.
<https://doi.org/10.1002/2014GL060310>

Stillman, D. E., Michaels, T. I., Hoover, R. H., Barth, E. L., Primm, K. M., Egan, A. F., & Grimm, R. E. (2021). Evaluation of grainflow mechanisms for martian recurring slope lineae (RSL). *Icarus*, 369 (114648). <https://doi.org/10.1016/j.icarus.2021.114648>

Tirsch, D., Jaumann, R., Pacifici, A., & Poulet, F. (2011). Dark aeolian sediments in Martian craters: Composition and sources. *Journal of Geophysical Research*, 116(E3).
<https://doi.org/10.1029/2009JE003562>

Verba, C. A., Geissler, P. E., Titus, T. N., & Waller, D. (2010). Observations from the High Resolution Imaging Science Experiment (HiRISE): Martian dust devils in Gusev and Russell craters. *Journal of Geophysical Research: Planets*, 115(E9), E09002.
<https://doi.org/10.1029/2009JE003498>

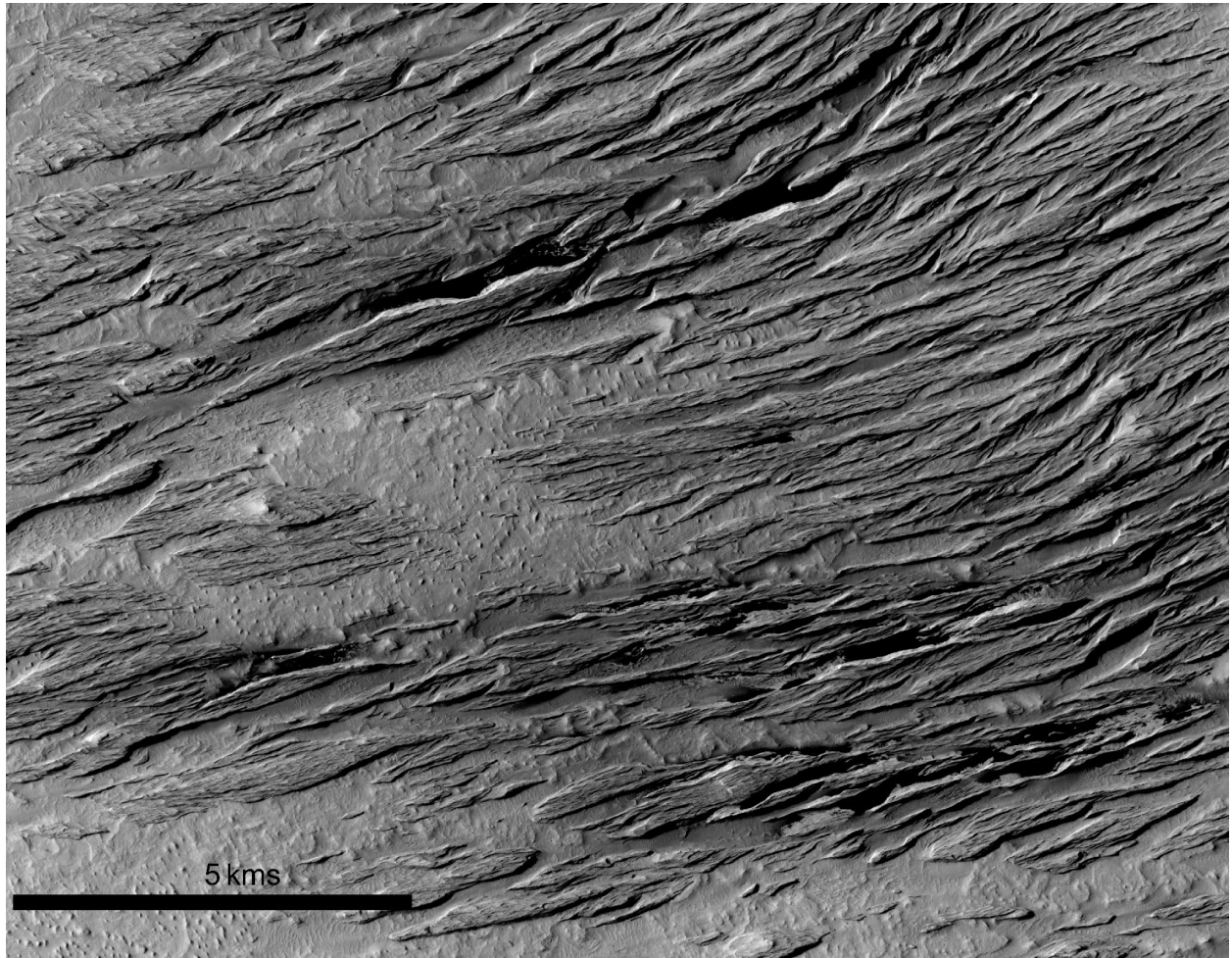
Viviano-Beck, C.E., Seelos, F.P., Murchie, S.L., Kahn, E.G., Seelos, K.D., Taylor, H.W., Morgan, M.F., (2014). Revised CRISM spectral parameters and summary products based on the currently detected mineral diversity on Mars. *J. Geophys. Res., Planets* 119 (6), 1403–1431

Viviano, C.E., Murchie, S.L., Daubar, I.J., Morgan, M.F., Seelos, F.P., Plescia, J.B., (2019). Composition of Amazonian volcanic material in Tharsis and Elysium, Mars, from MRO/CRISM reflectance spectra. *Icarus* 328, 274–286. <https://doi.org/10.1016/j.icarus.2019.03.001>.

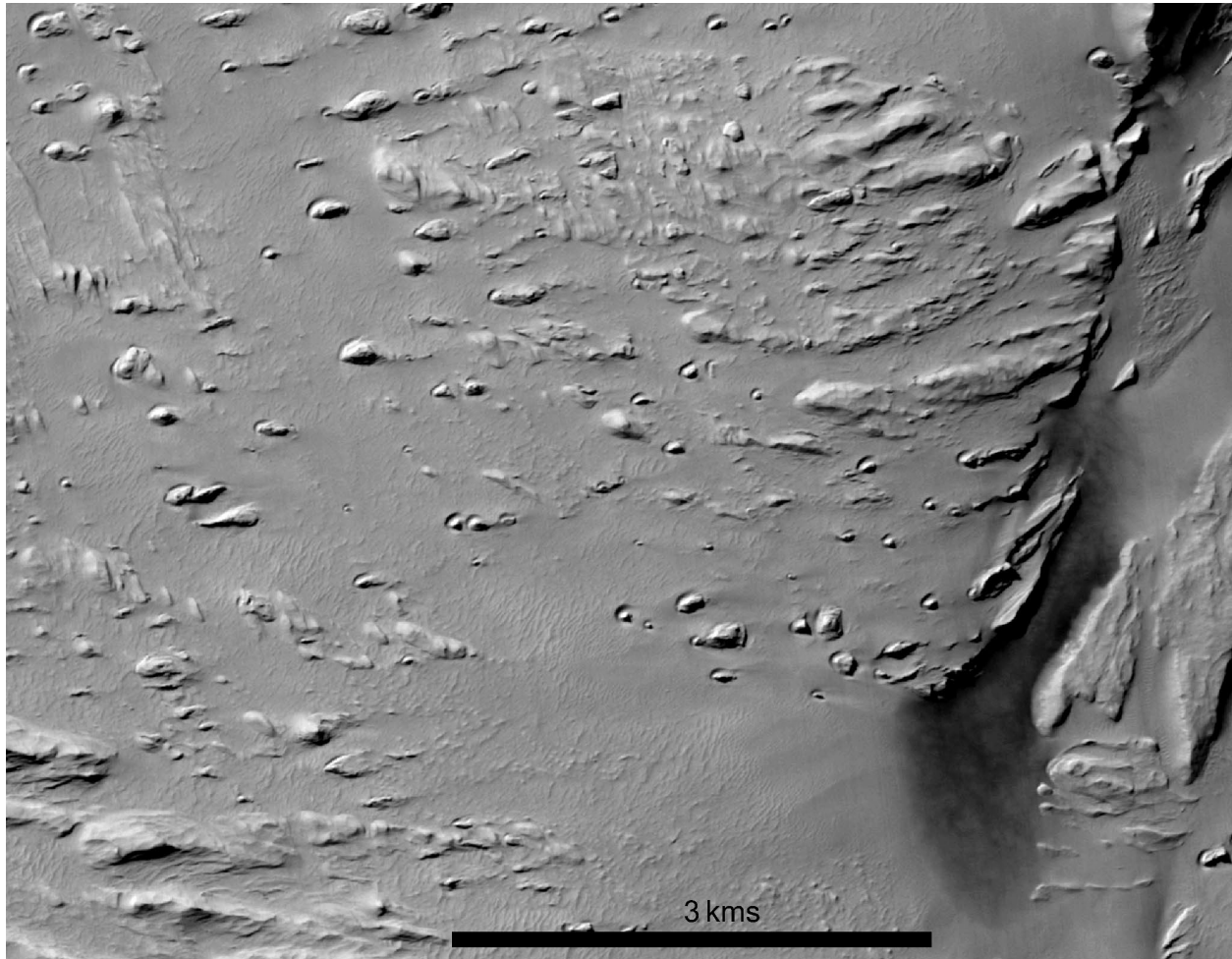
Zurek, R. W., and S. E. Smrekar (2007). An overview of the Mars Reconnaissance Orbiter (MRO) science mission, *J. Geophys. Res.*, 112, E05S01, doi:10.1029/2006JE002701.

Figure S1: Documentation of three aeolian morphologies in the Aeolis Dorsa study region. These images show evidence of aeolian abrasion of bedrock and deposition of sand and dust. All subfigures display CTM mosaic data (credit NASA/MSSS/JPL/Caltech Murray Lab (Dickson et al. 2018)).

- A) Yardangs in southern Zephyria Planum with dark sand in the yardang troughs. The yardangs are formed by aeolian erosion in one of the plana units, part of the Medusae Fossae Formation. Image is centered at 154.6°E -4.7°.



- B) Moats around the northern sides of knobs on eastern Aeolis Planum, formed within a plana unit, which is part of the MFF. Dark sand is visible towards the lower right of the image within a corridor between bedrock. This location of the dark sand and the albedo markings, indicative of dust devils, imply that wind acceleration and/or vorticity in this location has kept the sand mobile enough to remove some dust. The transition to a brighter land surface and the presence of moats, interpreted as scour marks that form in sand (Bishop, 2011), give evidence of dark sand underlying the bright surface. Image is centered at 150.54°E -5.4°.



- C) Sand-rich trough (white box) on central Zephyria Planum along a contact between planum unit, as inferred from the difference in surface texture and yardang characteristics below (to left) and above (to right) of the trough. Other nearby sandy deposits (black and brown boxes) are also indicated. Background image is centered at 154.5°E -0.5° with the location indicated by the red box labeled ‘Central Zephyria Planum’ on Figure 1C. Scale bar showing 20 kilometers applies to background image.

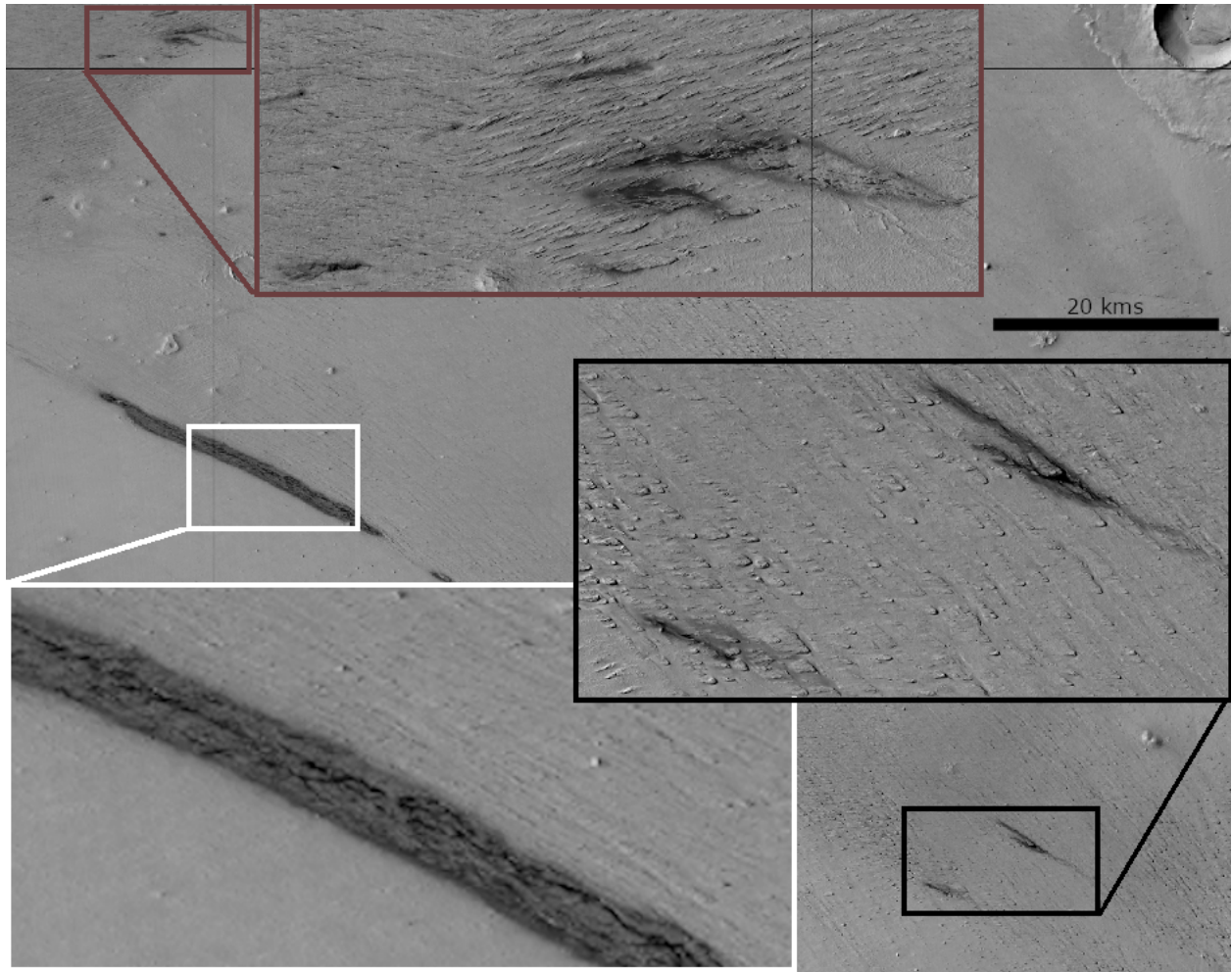


Figure S2: Average CRISM ratioed I/F spectra for the four potential sand source regions and two AD subregions (southern Zephyria Planum and Aeolis Chaos). Parenthetical value is the number of spectra extracted and averaged for each region. Plus and minus 1-sigma standard deviation shown for each spectrum in green. Y-scale identical for each plot to show variability in spectral contrast for each region. Weak spectral contrast in the Elysium Mons region likely due to heavy dust cover, and variability in spectral shapes in the Highlands spectra reflective of compositional diversity.

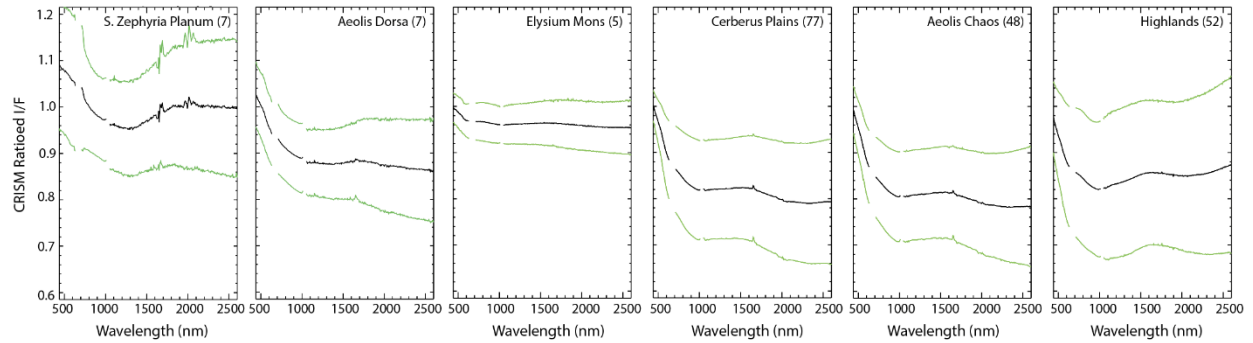
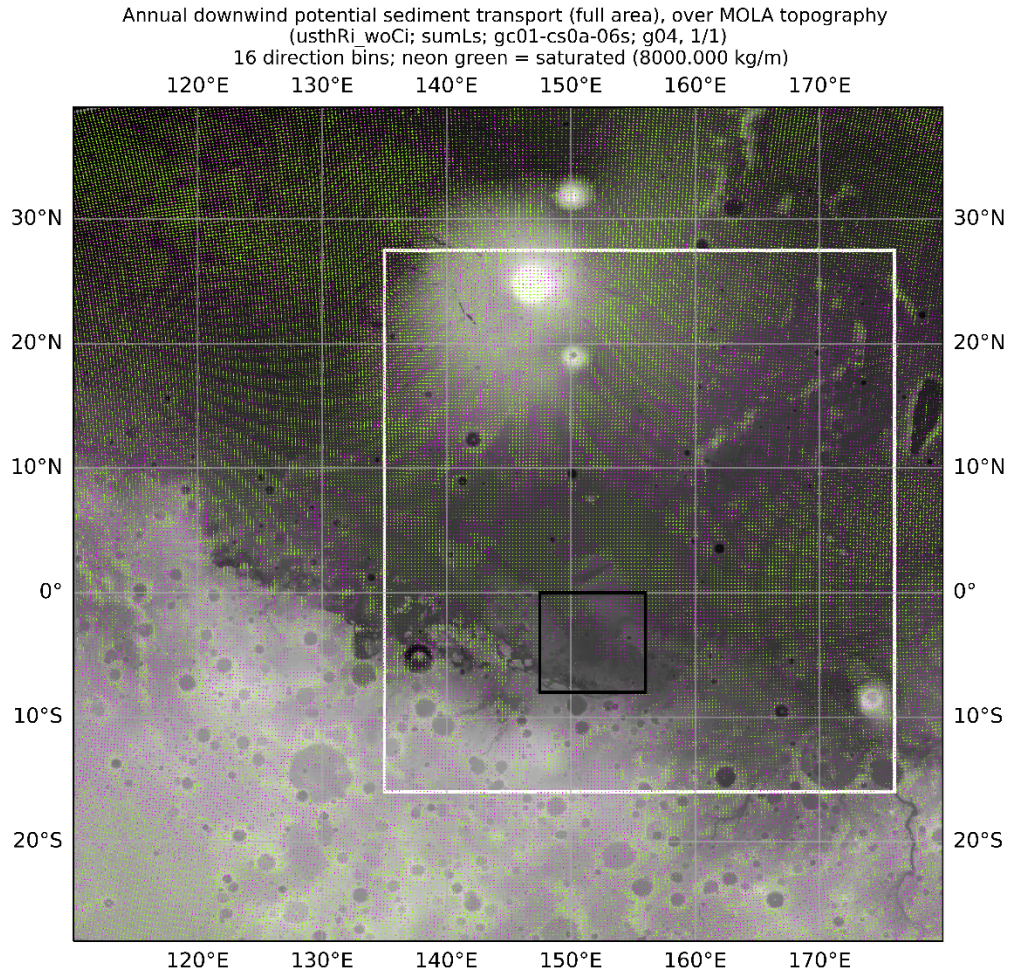
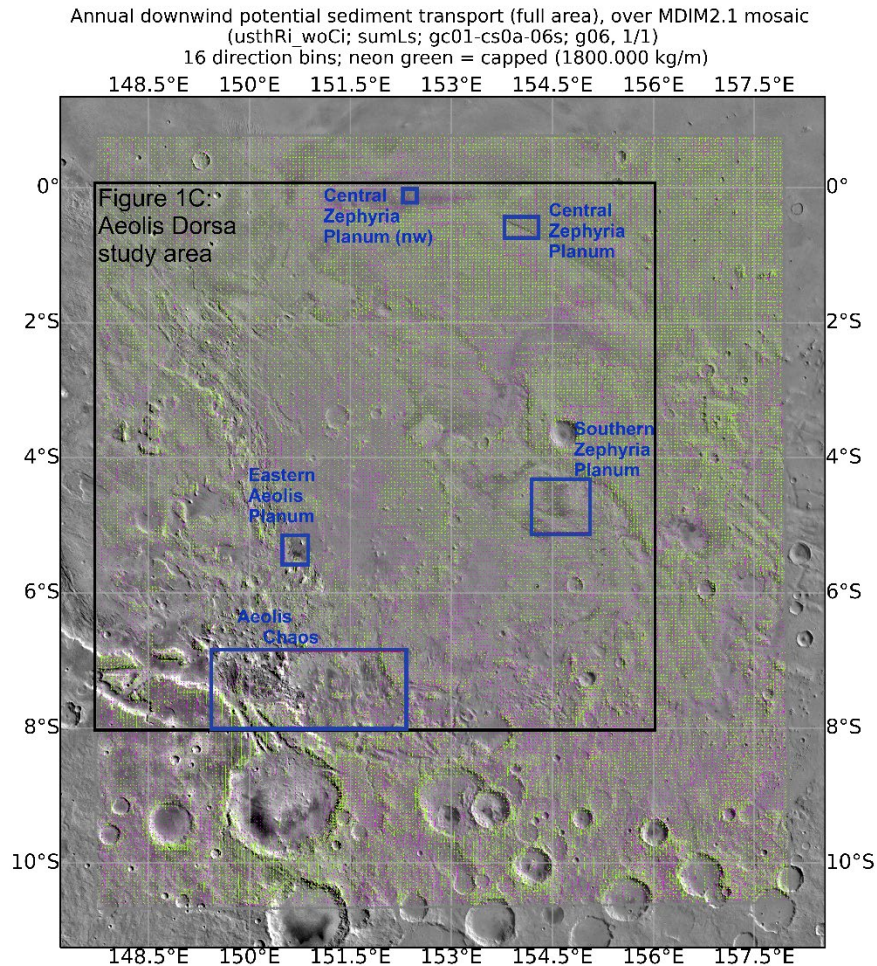


Figure S3: Seven representations of annual potential sand transport

A) View at full model resolution of Figure 3 in the manuscript, showing potential sand transport over the four potential sand source regions (Elysium Mons, Cerberus plains, southern highlands, and Aeolis Dorsa). Annual potential sand transport is presented as wind roses, with the vectors extending in the direction of transport (i.e., downwind). For discernibility of depositional locations, transport values are capped within one standard deviation of the mean value. These capped potential sand transport vectors (in green) indicate locations where sand could be removed or would be unlikely to deposit. The magnitudes of the other potential sand transport vectors (in pink), as shown by their relative lengths, indicate locations where sand deposition and sculpting are possible. The full model resolution is shown by the spacing of the vector plots, and topographic features below that resolution are not reflected in the model results. The capping value for annual potential sand transport at this location is 8000 kg m^{-1} . White box indicates the extent of the regional view shown in Figure 1B. Black box indicates the location of the Aeolis Dorsa study area shown in Figure 1C and Figure DR3b.

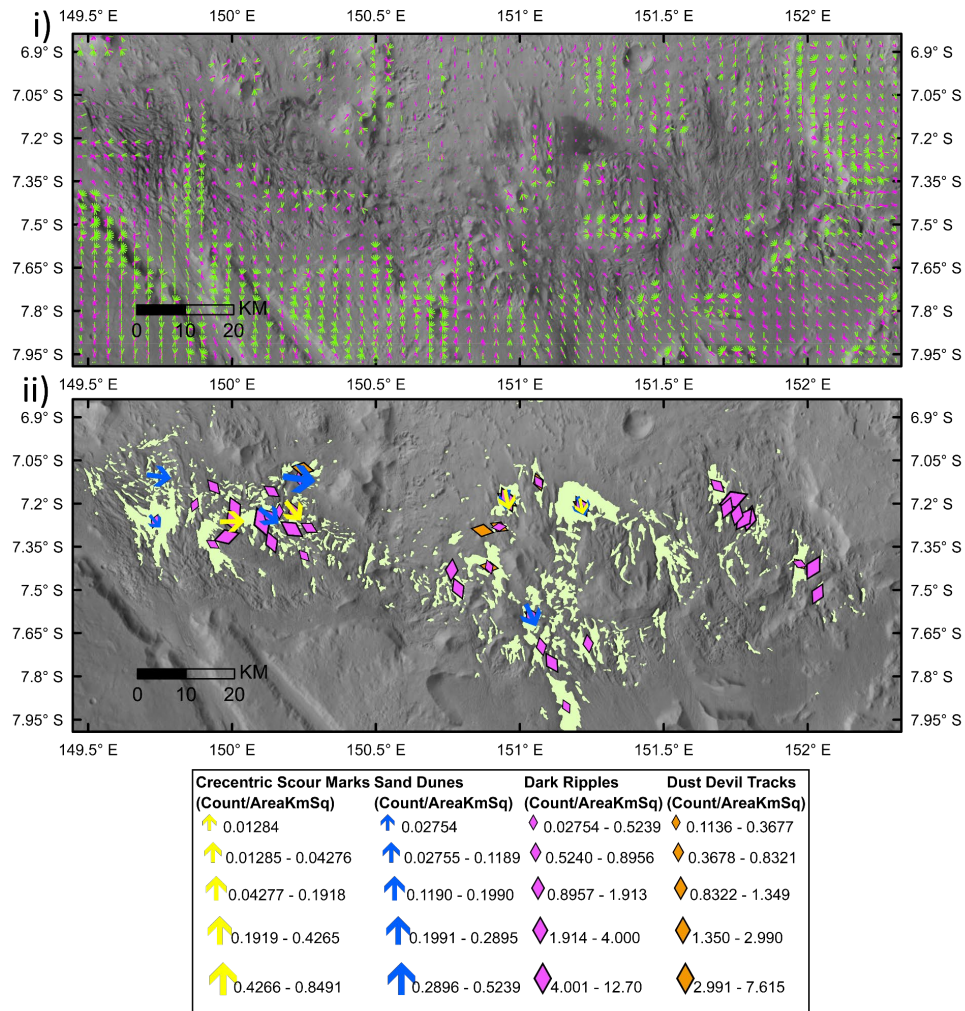


- B) View at full model resolution of potential sand transport vectors in the Aeolis Dorsa study area, plotted over the Viking MDIM2.1 mosaic. Black box, corresponding to the black box in Figure DR3a above, indicates the location of the Aeolis Dorsa study area shown in Figure 1C. Blue boxes, as on Figure 1C, indicate the locations of the subsequent Figure DR3 images, shown below. Visualization of annual potential sand transport is as indicated in the caption for Figure DR3a. The capping value for annual potential sand transport at this location is 1800 kg m^{-1} .

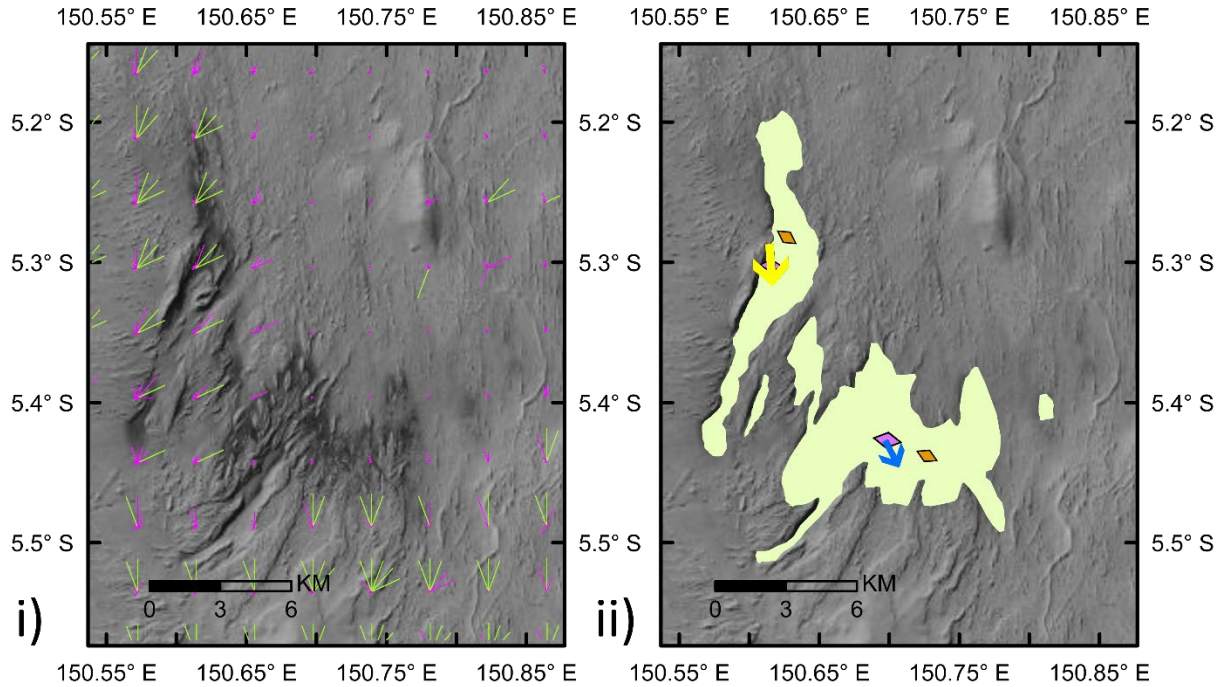


Each subsequent figure (Figures DR3c through g) consists of two panels showing the same sand-rich location in Aeolis Dorsa. For both panels, the basemap is a portion of the blended global mosaic (Dickson et al., 2018) of Context Camera images (Malin et al., 2007). The first panel (i) shows potential sand transport vectors. Visualization of annual potential sand transport is as indicated in the caption for Figure DR3a. For inter-comparability, we use the same capping value of 1800 kg m^{-1} for annual potential sand transport in all of these locations. The second panel (ii) shows the sand mapping (in light green) with sand mobilization directions inferred from mapping (see Methods). The data for these inferred wind directions are indicated by the symbologies shown in the panel and in the legends for each figure. Symbol sizes are scaled to the number of indicators per square kilometer of dark sand, providing a weighting function.

- C) Aeolis Chaos: Potential sand transport modeling indicates that Aeolis Chaos is currently a sand sink. Vectors along the southern margin of the depression show net northward transport. Vectors along the northern margin show mixed transport directions with a southward predominance. Vectors on the western margin show eastward transport. Vectors on the eastern margin show more mixed flow directions, including a westward component. A sediment transport pathway through the depression is not apparent and transport potential is minimal within the depression itself, implying deposition. Within the depression, the locations of mapped sand coincide with locations of minimal potential sand transport. The southward potential sand transport near 151.1°E, -7.7° is in agreement with the southward ripple motion detected in the Animation DR1, supporting the validity of the model output.

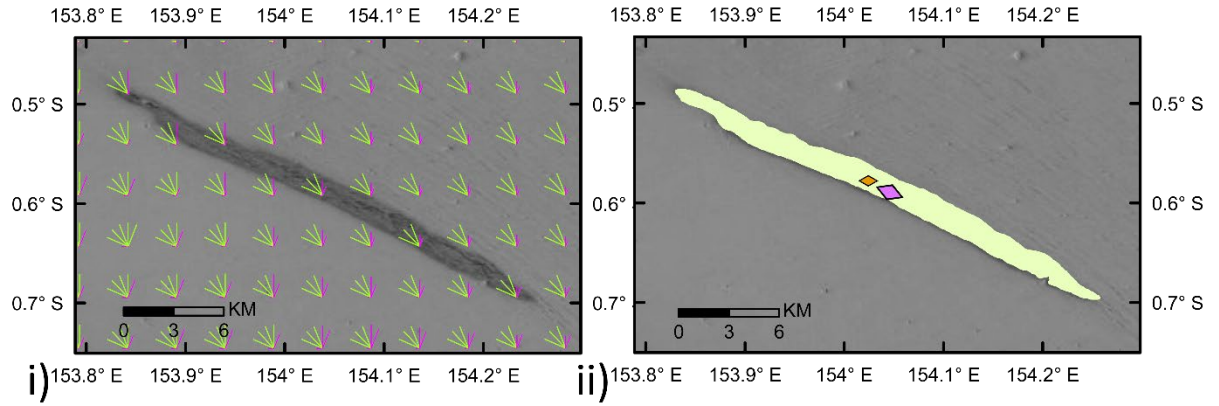


D) Eastern Aeolis Planum: The potential sand transport vectors indicate sand influx from the southwest with little potential flux in the center of the image, coincident with the location of the dark sand. Dust-covered sand is evidenced by scour marks around the margins of the visibly dark deposit, as mapped. Thus, we infer that the dark sand as mapped in this location is kept freer of dust by winds funneled through topographic features (Figure DR1b), below the model resolution.



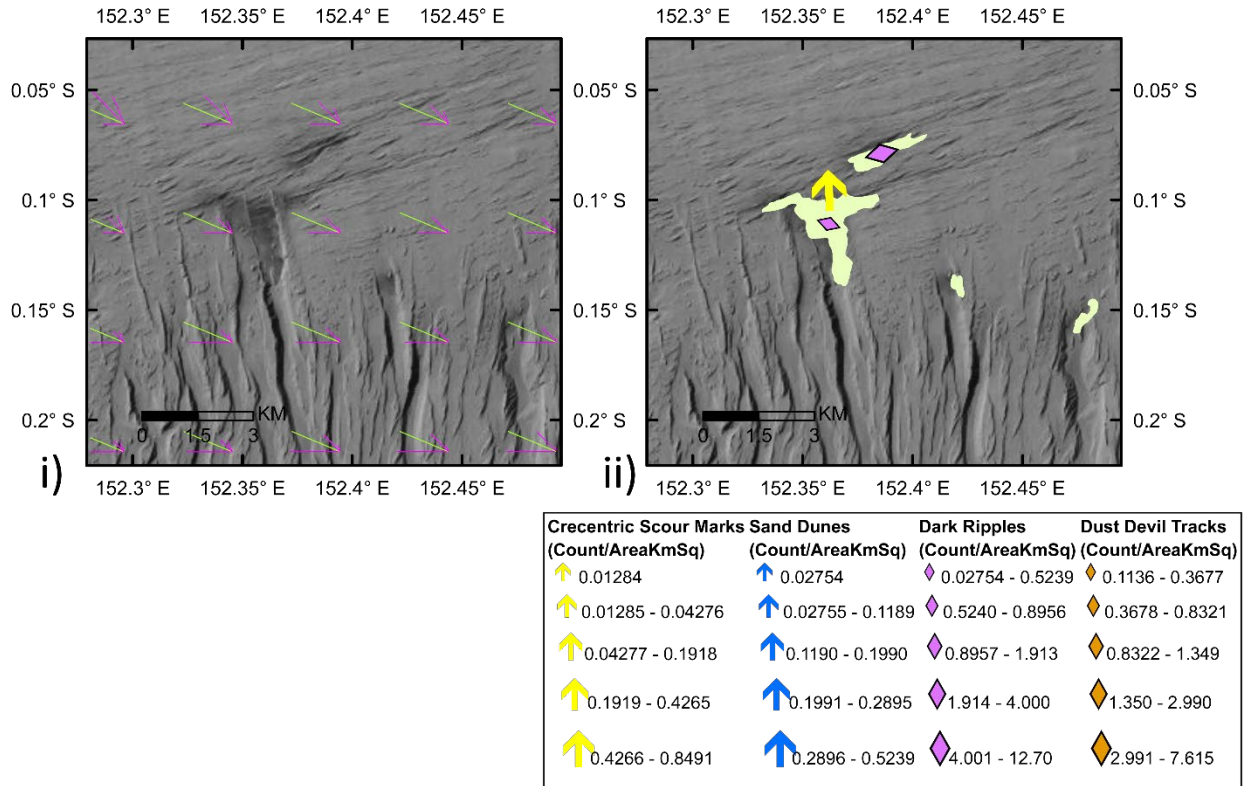
Crecentric Scour Marks (Count/AreaKmSq)	Sand Dunes (Count/AreaKmSq)	Dark Ripples (Count/AreaKmSq)	Dust Devil Tracks (Count/AreaKmSq)
↑ 0.01284	↑ 0.02754	◇ 0.02754 - 0.5239	◇ 0.1136 - 0.3677
↑ 0.01285 - 0.04276	↑ 0.02755 - 0.1189	◇ 0.5240 - 0.8956	◇ 0.3678 - 0.8321
↑ 0.04277 - 0.1918	↑ 0.1190 - 0.1990	◇ 0.8957 - 1.913	◇ 0.8322 - 1.349
↑ 0.1919 - 0.4265	↑ 0.1991 - 0.2895	◇ 1.914 - 4.000	◇ 1.350 - 2.990
↑ 0.4266 - 0.8491	↑ 0.2896 - 0.5239	◇ 4.001 - 12.70	◇ 2.991 - 7.615

- E) Central Zephyria Planum: The potential sand transport vectors show potential transport predominantly to the northwest, parallel to this linear ~20-m-deep trough. Transport directions that diverge from this trough-parallel direction all have some northward component. Any of the modeled directions would provide an influx of sand from the planum. Alternatively, the sand could be liberated by aeolian abrasion from the walls of the trough, which would likewise be a planum source.

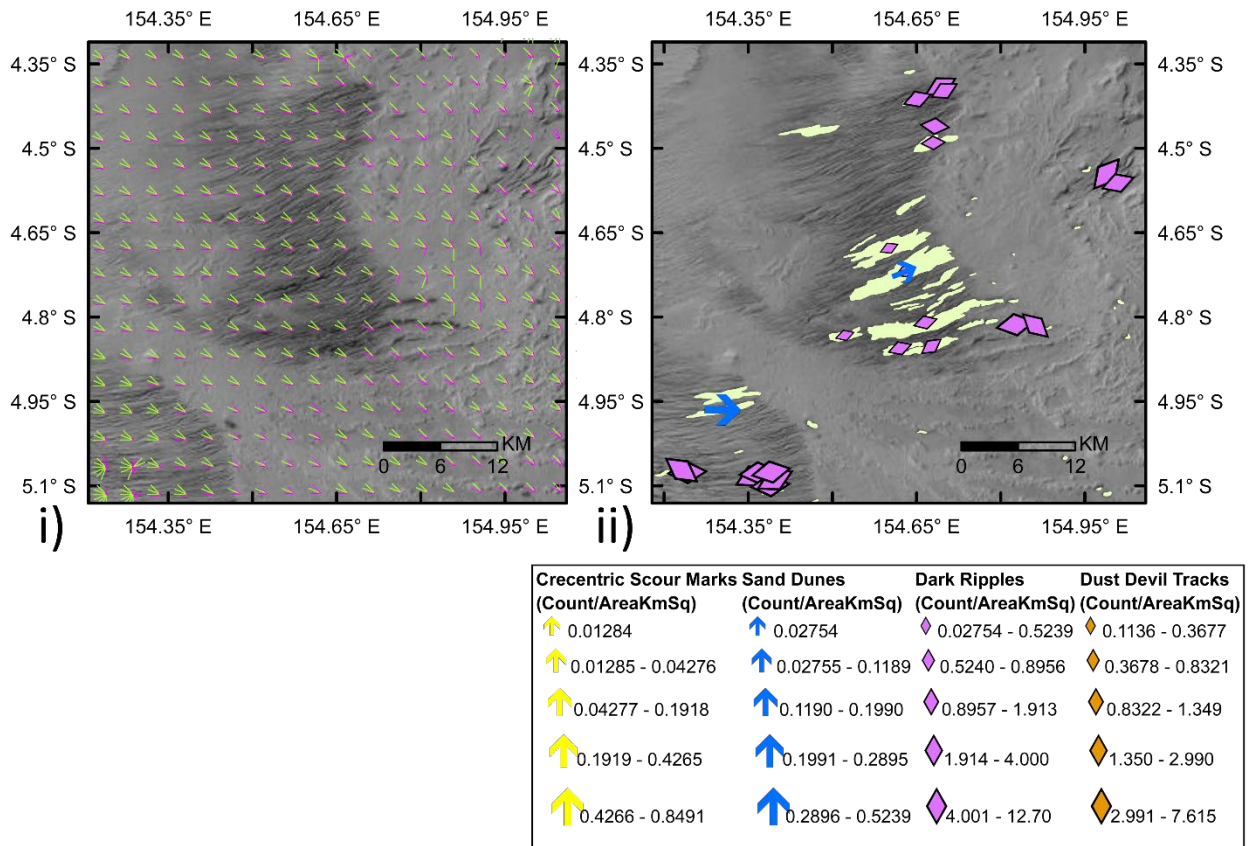


Crecentric Scour Marks (Count/AreaKmSq)	Sand Dunes (Count/AreaKmSq)	Dark Ripples (Count/AreaKmSq)	Dust Devil Tracks (Count/AreaKmSq)
↑ 0.01284	↑ 0.02754	◇ 0.02754 - 0.5239	◇ 0.1136 - 0.3677
↑ 0.01285 - 0.04276	↑ 0.02755 - 0.1189	◇ 0.5240 - 0.8956	◇ 0.3678 - 0.8321
↑ 0.04277 - 0.1918	↑ 0.1190 - 0.1990	◇ 0.8957 - 1.913	◇ 0.8322 - 1.349
↑ 0.1919 - 0.4265	↑ 0.1991 - 0.2895	◇ 1.914 - 4.000	◇ 1.350 - 2.990
↑ 0.4266 - 0.8491	↑ 0.2896 - 0.5239	◇ 4.001 - 12.70	◇ 2.991 - 7.615

F) Central Zephyria Planum (nw): As for Central Zephyria Planum, the potential sand transport modeling shows predominantly potential transport to the northwest, without any southward or eastward components. This sand-rich location sits on the south-facing slope of a broad ~100-meter-deep depression. The sand deposits are situated at the northern ends of yardangs and exhibit diffuse western margins, consistent with the northwestward potential sand transport. The only viable upwind source for sand in this location is the planum itself, as for the Central Zephyria Planum location (Figure DR3e). This planum source includes the possibility that sand is sourced from the yardang walls immediately adjacent to the deposits.



G) Southern Zephyria Planum: The potential sand transport vectors in this location are predominantly northwestward, approximately transverse to the yardangs. However, the best available input topographic data for the modeling was not sufficient to resolve the yardangs. Outside of the yardang fields, the scarce wind direction indicators from mapping show consistency with the model vectors. The orthogonal orientations of the potential sand transport and the yardangs suggest that minimal sand is entering or exiting the yardang field. Sand mobilization indicators from mapping imply flow along the yardang troughs. However, these troughs are anastomosing, providing limited ingress or egress pathways. The several potential sand source outcrops fully within the yardang field (Figure 4A) support the suggestion from modeling that sand within the troughs was generated from the yardang walls.



REFERENCES

Bishop, Mark A. 2011, Aeolian scours as putative signatures of wind erosion and sediment transport direction on Mars, *Geomorphology*, 125: 569-74.

Dickson, J.L., Kerber, L.A., Fasset, C.I. and Ehlmann, B.L., 2018, A global, blended CTX mosaic of Mars with vectorized seam mapping: a new mosaicking pipeline using principles of non-destructive image editing: Lunar and Planetary Science Conference XLIX, abstract 2480.

Malin, M. C., Bell, J.F., III, Cantor, B.A. and 11 others, 2007, Context Camera Investigation on board the Mars Reconnaissance Orbiter: *Journal of Geophysical Research—Planets*, v. 112, E05S04, doi:10.1029/2006JE002808.

Captions for Supplemental information uploaded separately:

- Animation S1: AnimationSI1_004125_039596_1720_RED_A_01_ORTHO_roi5.gif
This animation is a time-step sequence using co-located orthoimages from PSP_004125_1720 and ESP_039596_1720 of dark sand ripples in Aeolis Chaos demonstrating the cumulative effect of southward winds. Unambiguous ripple migration, although subtle, was detected in several adjacent areas as well and the wind directions are consistent with results from geomorphic mapping. Images are separated by 4.02 Mars years (7.57 Earth years). The location is centered at 151.1°E, -7.7°. See DTEEC_041086_1720_039596_1720_A01 at <https://hirise.lpl.arizona.edu/>. Image credit: NASA/JPL-Caltech/University of Arizona.
- Dataset S1 in Excel format: TableSI1_AeolisDorsa_CRISM_wANOVA.xlsx
This Excel spreadsheet provides the CRISM mineralogical identifications, their tabulation, and their statistical analysis demonstrating separability by composition among the four potential sand source regions. The first tab in the Table explains the spreadsheet structure and information content.
- Dataset S2 in Excel format: TableSI2_AeolisDorsa_HiRISE_PSS-survey.xlsx
This Excel spreadsheet provides the final results of a survey of HiRISE data (through December 2020) for potential sand sources in the Aeolis Dorsa region, 147.5-150°E, 0-8°S. The tab “on Plana units, High Conf Level” includes in column P images showing all the potential sand sources with four or five of five characteristics of potential sand source outcrops.
- CRISM browse products: AeolisDorsa_CRISM_browse.zip:
This file contains the CRISM browse products located in southern Zephyria Planum created for this work. Images are color composites of three parameters, namely, R: BDI1000VIS, G: BD1300, B: BDI1000IR
- ArcGIS geodatabase with layer files: AeolisDorsaSand.gdb.7z
The file containing the geodatabase created in this research with i) CRISM identifications, ii) Sand mapping, iii) SI_image_locations, iii) HiRISE potential sand source survey results, iv) Plana units from Burr et al., 2021, Aeolis Dorsa USGS map, v) locations of grain size derivations from thermal inertia, and vi) line density map of regions with clustered sand.
- ArcGIS geodatabase with locations of grain size derivation: AeolisDorsaSand_grain-size.gdb.7z
The file containing the geodatabase created in this research with the locations where grain size was derived from thermophysical data.

